

Adaptive Hierarchical Tensor Product Finite Elements for Fluid Dynamics

S.-A. H. Schneider¹, Chr. Zenger²

Institut für Informatik, Technische Universität München, D-80290 München, Germany; e-mail: {schneids,zenger}@in.tum.de

Received: 10.08.2000/ Revised version: 10.08.2000

To Prof. Dr. Chr. Zenger 60th birthday.

Summary. This article is a contribution to the current research field of computational fluid dynamics. We discretize the Stokes flow for $Re = 0$ with adaptive hierarchical finite elements and verify the method with numerical results for the three-dimensional lid-driven cavity problem. In order to solve the corresponding Stokes problem, we replace the constraint of the conservation of mass by an elliptic boundary value problem for the pressure distribution p . Consequently, the solution of the Stokes problem is reduced to the solution of $d + 1$ Poisson problems, the so-called successive poisson scheme. We use the hierarchical tensor product finite element method for the numerical solution of the Poisson problems as a basic module. On one hand, this allows a straightforward approach for the self-adaptive solution process: We start with a regular discretization and create new elements, where the hierarchical surplus of the weak divergence indicates the need to refine. On the other hand, we use multigrid concepts for the efficient solution of the large linear systems arising from the elliptic differential equations. The discussed example shows that the use of elements with variable aspect ratio pays off for the resolution of line singularities.

Key words: hierarchical finite elements, lid-driven cavity, sparse grids, successive poisson scheme, Stokes flow, tensor product approach

Mathematics Subject Classification (1991): 65N22, 65N30, 65N50, 65N55

1. Introduction

The first known mathematician to use hierarchical ideas was Archimedes in *Τετραγωνισμὸς παραβολῆς* (the quadrature of the parabola), see [21]. By inductively exhausting the parabola with triangles, he was able to measure the area given by a parabola, see Fig. 1. In

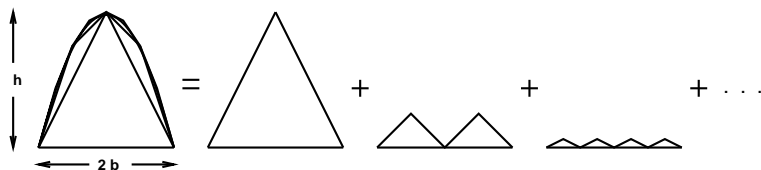


Fig. 1. Archimedes' idea to calculate the area A under the parabola with height h and base $2b$ by inductively filling up with triangles: $A = hb \left(1 + \frac{1}{4} + \frac{1}{16} + \dots\right) = hb \frac{4}{3}$.

1909, Faber [5] introduced the hierarchical basis and explicitly used it for the representation of functions. Yserentant [24] applied the hierarchical basis in 1986 as a preconditioner. In 1990, Zenger [25] directly represented a smooth multivariate function u with a hierarchical tensor product basis instead of a standard nodal basis. The coefficients of this representation, the so-called *hierarchical surplusses*, decrease with the volume of the support of the corresponding basis functions. Consequently, the hierarchical surplus is a very simple criterion for the decision of whether the contribution to the basis representation is important enough or not. These considerations lead to the concept of *sparse grids* in which we order the basis functions in terms of their contribution to the basis representation and, with that, in terms of their support volume. It turns out that sparse grids are a priori L_2 - or H^0 -adaptive grid structures and lessen the so-called “curse of dimension”, see Bungartz [2]. To get a rough idea, let us compare the number of grid points that are necessary to reduce, e.g., the L_2 -error of a linear finite element discretization by a factor $1/4$ for a sufficiently smooth problem. Supposing additional regularity conditions, in a standard nodal approximation space, we asymptotically need 2^d and in the sparse grid approximation only twice – independent of the dimension d – as many grid points. Based on this concept, an adaptive hierarchical finite element method is presented in [15]. Using duality arguments, a user specified adaptation criterion allows an efficient discretization of a given problem. The aim of this article is to apply

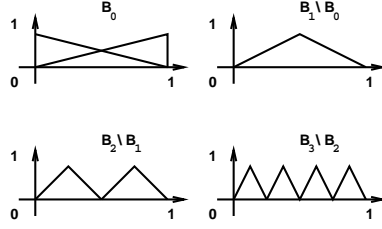


Fig. 2. The one-dimensional piecewise linear hierarchical basis: basis functions of the bases B_0, \dots, B_3 .

these results to a three-dimensional example: the three-dimensional lid-driven cavity problem. We discuss the discretization of the corresponding Stokes problem and formulate the solution algorithm.

2. Hierarchical Finite Elements

Beginning with the one-dimensional case, we construct the *hierarchical basis* B_n of *depth* n for the interval $\Omega^{(1)} := [0, 1]$ from the standard hat function $\phi : \mathbb{R} \rightarrow \mathbb{R}$,

$$\phi(x) := \begin{cases} 1 - |x| & \text{for } x \in [-1, +1], \\ 0 & \text{otherwise,} \end{cases}$$

and the linear transformation $\tau_{x_j} : [x_j - h_{x_j}, x_j + h_{x_j}] \rightarrow [-1, 1]$ defined by $\tau_{x_j}(x) := (x - x_j)/h_{x_j}$. All piecewise linear basis functions $\phi_{x_j} \in B_n$ can then be constructed by dilation and translation of ϕ

$$\phi_{x_j}(x) := \phi(\tau_{x_j}(x)) \quad \forall x \in [x_j - h_{x_j}, x_j + h_{x_j}],$$

with $\text{supp } \phi_{x_j} := [\max\{0, x_j - h_{x_j}\}, \min\{x_j + h_{x_j}, 1\}] \subset [0, 1]$ for certain given discretization points $x_j \in \Omega^{(1)}$ and the corresponding grid width $0 < h_{x_j} \in \mathbb{R}$. We call $x_j \in [0, 1]$ the *basis point* $bp(\phi_{x_j})$ of the basis function $\phi_{x_j} \in B_n$.

Let us construct the hierarchical basis B_n inductively, starting with $B_0 := \{\phi_0(x) := 1 - x, \phi_1(x) := x\}$, where we define $h_0 := h_1 := 1$, see Fig. 2, by two principles:

1. the *principle of hierarchy*: the family of bases $B_n \forall n \geq 0$ build a nested sequence of sets by $B_{n-1} \subset B_n \forall n > 0$ and
2. the *principle of surplus*: all basis functions of $B_n \forall n > 0$ may not influence the representation of the function $u \in H^1(\Omega^{(1)})$ in any basis point $x_j \in bp(B_{n-1})$ of the basis functions of B_{n-1} .

The second principle gives a hint how to construct the basis functions of $B_n \forall n > 0$. All basis functions $\phi_{x_j} \in B_n \setminus B_{n-1}$ have to fit with their support exactly in the set of intervals one gets by the partition of $\Omega^{(1)}$ by the basis points x_j of the basis functions $\phi_{x_j} \in B_{n-1}$.

In Fig. 2, the first three steps of constructing B_n are given. For example, one deduces the only basis function $\phi_{1/2} \in B_1 \setminus B_0$ by exhausting the interval $[0, 1]$ by the support $\text{supp } \phi_{1/2}$ of the function $\phi_{1/2}(x) := 1 - |2x - 1|$ with $h_{1/2} := 1/2$. It is easy to deduce that for all basis functions $\phi_{x_j} \in B_n \setminus B_{n-1} \forall n \geq 1$ hold for the grid width $h_{x_j} := 2^{-n}$, and therefore, the support of the basis function ϕ_{x_j} has the length 2^{1-n} .

Now, we exploit the *tensor product* approach for the d -dimensional case and give a recursive formulation of the d -dimensional hierarchical basis $B_{\mathbf{n}^d}^{(d)}$ for $d > 1$

$$B_{\mathbf{n}^d}^{(d)} := B_{\mathbf{n}^{d-1}}^{(d-1)} \otimes B_{n_d},$$

where we define $\mathbf{n}^d := (n_1, \dots, n_d) \in N_0^d$. We start the recursion with $B_{n_1}^{(1)} := B_{n_1}$. The indices n_i $i = 1, \dots, d$ indicate the depths of the basis $B_{\mathbf{n}^d}^{(d)}$ in the directions i . In the following considerations, we suppress the upper dimension index (d) whenever the dimension d is clear from the context. The piecewise multilinear basis functions are defined as

$$\begin{aligned} \phi_{\mathbf{x}_j}^{(d)}(\mathbf{x}^{(d)}) &:= \phi_{\mathbf{x}_j}^{(d-1)}(\mathbf{x}^{(d-1)}) \cdot \phi_{x_{j_d}}^{(1)}(x_{j_d}^{(1)}) \\ &:= \prod_{i=1}^{d-1} \phi_{x_{j_i}}(x_i) \cdot \phi_{x_{j_d}}(x_d) \\ &= \prod_{i=1}^d \phi_{x_{j_i}}(x_i), \end{aligned}$$

where $\mathbf{x}^{(d)} := (x_1, \dots, x_d) \in \Omega^{(d)} := [0, 1]^d$. The coordinates of the basis point $\mathbf{x}_j := (x_{j_1}, \dots, x_{j_d})$ of the d -dimensional basis function $\phi_{\mathbf{x}_j}$ are given by the d basis points of B_{n_i} of the corresponding one-dimensional basis functions in all directions $i = 1, \dots, d$, see also the *subspace scheme* in Fig. 3. To get an impression of a typical two-dimensional basis function, see Fig. 4. The space spanned by $B_{\mathbf{n}^d}^{(d)}$ is called $V_{\mathbf{n}^d}^{(d)} := \langle B_{\mathbf{n}^d}^{(d)} \rangle \subset V = H^1(\Omega^{(d)})$. Note that $V_{\mathbf{n}^d}^{(d)}$ is also generated by a classical tensor nodal basis with 2^{n_i+1} basis functions in direction $i = 1, \dots, d$.

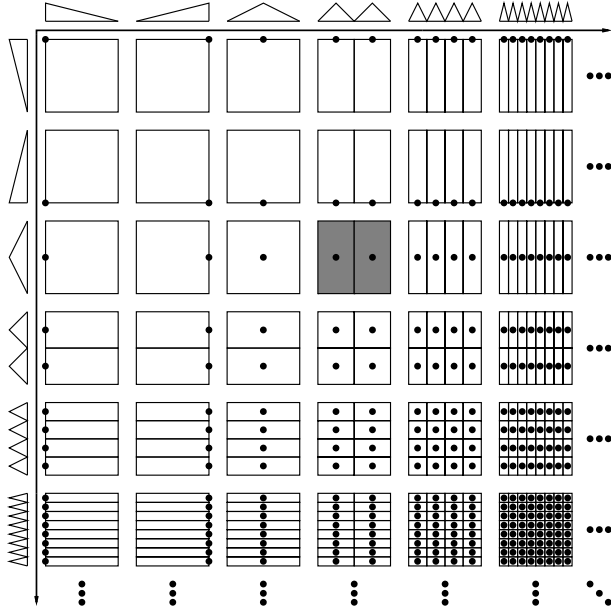


Fig. 3. The multidimensional piecewise linear hierarchical basis: two-dimensional subspace scheme with supports $\text{supp } \phi_{\mathbf{x}_j}$ and basis points \mathbf{x}_j of the corresponding hierarchical basis function $\phi_{\mathbf{x}_j}$. (For example, the hierarchical basis functions with the grey supports are displayed in Fig. 4.)

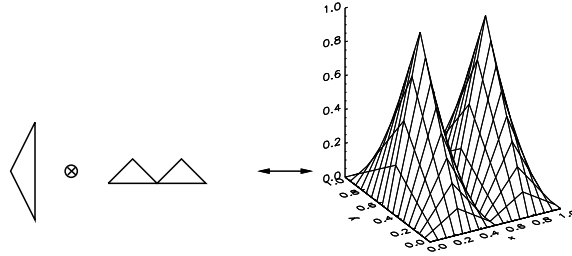


Fig. 4. The multidimensional piecewise linear hierarchical basis: illustration of the tensor product approach for piecewise bilinear basis functions. The corresponding supports are shown in Fig. 3 (grey).

Any function u of the space $V_{\mathbf{n}^d}^{(d)}$ has the *hierarchical basis representation*

$$u_{\mathbf{n}^d}(\mathbf{x}) = \sum_{\mathbf{x}_j \in bp(B_{\mathbf{n}^d}^{(d)})} u_{\mathbf{n}^d, \mathbf{x}_j}^{\text{hier}} \phi_{\mathbf{x}_j}(\mathbf{x}),$$

with $u_{\mathbf{n}^d, \mathbf{x}_j}^{\text{hier}} \in \mathbb{R} \forall \phi_{\mathbf{x}_j} \in B_{\mathbf{n}^d}^{(d)}$. The coefficients $u_{\mathbf{n}^d, \mathbf{x}_j}^{\text{hier}}$ correspond to the increments of data coming from the basis function $\phi_{\mathbf{x}_j}$, and therefore, they are also called *hierarchical surplusses*.

As a model problem, we consider Poisson's equation with Dirichlet and Neumann boundary conditions

$$(1) \quad \begin{aligned} -\Delta u &= f \text{ in } \Omega^{(d)}, \\ u &= g \text{ on } \emptyset \neq \Gamma_D \subset \Gamma := \partial\Omega^{(d)}, \\ \partial_\nu u &= m \text{ on } \Gamma_N := \Gamma \setminus \Gamma_D. \end{aligned}$$

Let us denote the standard L_2 -inner product by $(\cdot, \cdot)_X$ and by $\|\cdot\|_X$ the corresponding norm on $\Omega^{(d)}$, resp. Γ . The *weak* or *variational formulation* of (1) reads then

$$(2) \quad (\nabla \phi, \nabla u)_\Omega = (\phi, f)_\Omega + (\phi, m)_\Gamma \quad \forall \phi \in V.$$

We also call (2) the *continuous primal problem*. Using the finite element method, we obtain an approximation $u_n \in \langle A_n \rangle$ of the analytical solution $u \in V$ in the *ansatz space* $\langle A_n \rangle \subset V$ by solving the *discrete primal problem* of (2) given by

$$(\nabla \phi, \nabla u_n)_\Omega = (\phi, f_n)_\Omega + (\phi, m_n)_\Gamma \quad \forall \phi \in T_n,$$

where $\langle T_n \rangle \subset V$ is called the *test space*. Sticking to a Ritz-Galerkin approach, we choose $T_n = A_n \subset B_{\mathbf{n}^d}^{(d)}$. The discretization underlies the *grid* $G_n := bp(A_n)$.

The function $u_n = \sum_{\mathbf{x}_j \in bp(A_n)} u_{n, \mathbf{x}_j} \cdot \phi_{\mathbf{x}_j}$ interpolates the Dirichlet boundary value function g on $\Gamma \cap bp(A_n)$, $f_n = \sum_{\mathbf{x}_j \in bp(A_n)} f_{n, \mathbf{x}_j} \cdot \phi_{\mathbf{x}_j}$ interpolates the source function f in $\Omega^{(d)} \cap bp(A_n)$ and $m_n = \sum_{\mathbf{x}_j \in bp(A_n)} m_{n, \mathbf{x}_j} \cdot \phi_{\mathbf{x}_j}$ interpolates the Neumann boundary value function m on $\Gamma_N \cap bp(A_n)$. We end up with a system of linear equations $S \cdot u_n = b_n$ for the coordinate vector $u_n := (u_{n, \mathbf{x}_j})_{\mathbf{x}_j \in bp(A_n)} \in \mathbb{R}^N$ of the function u_n . We correspondingly define the coordinate vectors $f_n := (f_{n, \mathbf{x}_j})_{\mathbf{x}_j \in bp(A_n)} \in \mathbb{R}^N$ of the source function f and $m_n := (m_{n, \mathbf{x}_j})_{\mathbf{x}_j \in bp(A_n)} \in \mathbb{R}^N$ of the Neumann boundary function. The vector b_n then is the *load vector*. The matrix S is known as the *stiffness matrix* with entries $s_{\mathbf{x}_k, \mathbf{x}_j}$ defined for the bases functions $\phi_{\mathbf{x}_k} \in T_n$ and $\psi_{\mathbf{x}_j} \in A_n$; $S = (s_{\mathbf{x}_k, \mathbf{x}_j})_{\mathbf{x}_k \in bp(T_n), \mathbf{x}_j \in bp(A_n)} \in \mathbb{R}^{N \times N}$ and $s_{\mathbf{x}_k, \mathbf{x}_j} = (\nabla \phi_{\mathbf{x}_k}, \nabla \psi_{\mathbf{x}_j})_{\Omega^{(d)}}$.

3. Discretization of the Stokes Equations

We consider the d -dimensional domain $\Omega := [0, 1]^d$ with boundary $\Gamma := \partial\Omega$. The variables $u_i : \Omega \rightarrow \mathbb{R}$ $i = 1, \dots, d$ describe the *velocity field* $\mathbf{u} := (u_1, \dots, u_d) \in \mathbb{R}^d$ and the scalar $p : \Omega \rightarrow \mathbb{R}$ the *pressure*. The *Stokes equations* describe an incompressible, steady state and laminar flow, with the *kinematic viscosity* $\nu \in \mathbb{R}$, wherein the influence of convection is assumed to be small (density $\rho = 0$)

$$(3) \quad -\nu \Delta u_i + \partial_{x_i} p = 0 \quad \text{on } \Omega, \quad i = 1, \dots, d$$

$$(4) \quad \sum_{i=1}^d \partial_{x_i} u_i = 0 \quad \text{on } \Omega,$$

with appropriate boundary conditions for the velocity field \mathbf{u}

$$(5) \quad u_i|_{\Gamma} = u_{0,i} \text{ or } \partial_{x_j} u_i|_{\Gamma} = u_{0,i,j} \quad \forall i, j = 1, \dots, d.$$

Equation (3) describes the conservation of momentum. Equation (4) is derived from the conservation of mass.

A principal requirement in the solution of the Stokes equation (3) and (4) is the determination of the pressure distribution p . Therefore, we build the divergence of the momentum equations (3) Using (4), this leads to the Laplace equation for the pressure

$$(6) \quad -\Delta p = 0 \quad \text{on } \Omega.$$

Equation (6) defines an elliptic boundary value problem, hence boundary conditions are needed. The Dirichlet boundary condition is available only at an inlet and given by

$$(7) \quad p|_{\Gamma \cap \text{inlet}} = p_0.$$

On all other parts of the boundary Γ , we therefore use the divergence equation (4) prescribing normal derivatives of the velocity components u_j

$$(8) \quad \partial_{x_j} u_j|_{\Gamma} = - \sum_{i=1, i \neq j}^d \partial_{x_i} u_i \quad j = 1, \dots, d$$

on the surface Γ orthogonal to the direction j^1 . Note that, in case of Dirichlet boundary conditions (5), the derivatives $\partial_{x_i} u_i$ for $i \neq j$ can be analytically computed.

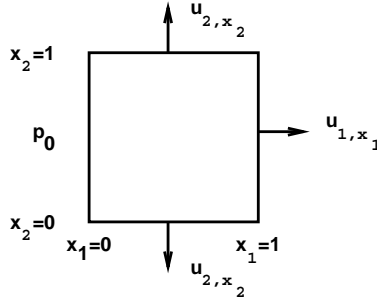


Fig. 5. The two-dimensional channel flow: required boundary conditions for the elliptic boundary value problem (6) for the pressure distribution p : Dirichlet boundary conditions p_0 on the inlet $x_1 = 0$ according to (7) and normal derivatives $\partial_{x_j} u_j|_F$, $j = 1, 2$ for the velocity field \mathbf{u} on $x_1 = 1$, $x_2 = 0$, and $x_2 = 1$ according to (8).

In Fig. 5 we give the additional boundary conditions for the two-dimensional channel flow as an example.

In summary, one can say that the solution of the Stokes problem (3) and (4) suffices the $d + 1$ equations given in (3) and (6) with the boundary conditions (5) and (8) for the velocity field \mathbf{u} and (7) for the pressure p .

3.1. The Discretization

In this subsection, we give a primitive variable Galerkin formulation of the Stokes problem. By the standard finite element arguments, we establish from (3) for the velocity field \mathbf{u} and from (6) for the pressure p the following weak formulation: find $u_i \in H^1(\Omega)$ $i = 1, \dots, d$ and $p \in H^1(\Omega)$ such that

$$(9) \quad \sum_{j=1}^d (\partial_{x_j} v, \partial_{x_j} u_i)_{\Omega} = \frac{1}{\nu} (\partial_{x_i} v, p)_{\Omega} \quad \forall v \in H^1(\Omega), i = 1, \dots, d,$$

$$(10) \quad \sum_{j=1}^d (\partial_{x_j} v, \partial_{x_j} p)_{\Omega} = 0 \quad \forall v \in H^1(\Omega)$$

hold.

¹ Note that we could use other boundary conditions, too, e.g. Neumann boundary conditions for the pressure p . However, the corresponding numerical results were oscillating.

We discretize the continuous formulation of the Stokes problem (9) and (10). Therefore, we choose the test and ansatz bases $T_n, A_n \subset H^1(\Omega)$ introduced in Section 2. In the following considerations, we discuss the case for the Dirichlet boundary conditions for the velocity. With the notation used there, we end up with a system of linear equations

$$(11) \quad Su_i = \frac{1}{\nu} K_i p \quad i = 1, \dots, d$$

$$(12) \quad Sp = 0.$$

We incorporate the boundary condition (5) for the velocity field \mathbf{u} in (11) and the Dirichlet boundary condition (7) for the pressure p in (12). The additional boundary conditions (8) are used for the coupling of the equations (11) and (12) in an outer iteration. Therefore, we start the solution of equation (12) in the first iteration step with arbitrary Dirichlet boundary values $p^0|_{\Gamma \setminus \text{inlet}}$ on the remaining boundary. In the following iteration steps, we correct these boundary values $p^0|_{\Gamma \setminus \text{inlet}}$ with the residuals of the *discrete weak divergence* according to (4)

$$(13) \quad \sum_{i=1}^d K_i u_i.$$

This means that the outer iteration corrects the Dirichlet boundary values $p^0|_{\Gamma \setminus \text{inlet}}$ of the pressure distribution p until the divergence equation is guaranteed also on the remaining boundary. Because equation (6) is a consequence of (10) the divergence equation holds also in the interior of Ω .

The numerical solution of the original Stokes problem given by (3) and (4) is reduced to a sequence of $d + 1$ Poisson equations (11) and (12) with Dirichlet boundary conditions. Hereby equation (11) results from the divergence equation. For the update of the Dirichlet boundary values of the pressure p , we use the weak divergence (13). Therefore, the divergence equation holds in the interior of Ω and on $\Gamma \setminus \text{inlet}$. We start the iteration with initial guesses for the velocity \mathbf{u}^0 and the pressure p^0 . For the outer iteration see Algorithm 1 “Successive Poisson Equation”. We get a sequence of solutions for the values of the velocities u_i^k , $i = 1, \dots, d$, and the pressure p^k for $k = 0, 1, \dots, k_{\max}$. So far, the convergence of the outer iteration has only been observed numerically. In all computations we had no problems with oscillating solutions.

Algorithm 1 Successive Poisson Equation

```

 $\mathbf{u}^0$  and  $p^0$  {initial guesses}
for  $k = 0$  to  $k_{\max}$  do
  solve (11) for  $\mathbf{u}^{k+1}$  with  $p^k$  {Dirichlet and Neumann conditions (5) }
  correct the Dirichlet conditions  $p^{k+1}|_{\Gamma \setminus \text{inlet}}$  {weak divergence (13) }
  solve (12) for  $p^{k+1}$  {Dirichlet condition (7) for the inlet  $p^{k+1}|_{\Gamma \cap \text{inlet}}$ }
end for

```

3.2. The Adaptation

We use the adaptivity tools developed in [15]. A refined discretization creates new grid points where the hierarchical surplus of the residuals of the weak divergence (13) indicates the need to refine. All calculations, that are the solution of the Poisson problems and the computation of the weak divergence, are carried out on the same grid structure, starting with a full grid with depth $t_0 = 2$ or $t_0 = 3$.

In the presented numerical example, we have artificial singularities in the corners due to the prescribed boundary values. These singularities are dominating the grid refinement. Therefore, it turned out to be useful to fix the depth t for the refinement steps, until no new grid points are created. After that, we increase the allowed maximum depth t by 1, and start the refinement process again, see also Algorithm 2 “Adaptive Stokes”. This ensures that not only the final

Algorithm 2 Adaptive Stokes

```

construct an initial coarse grid  $G_0$  {here a full grid of depth  $t_0 = 2, 3$ }
 $k := 0$ 
for  $t = t_0$  to  $t_{\max}$  do
  repeat
    solve the discrete problem on grid  $G_k$  {thereto see the Algorithm 1}
    compute the weak divergence (13) for each element in  $G_k$ 
    decide which elements have to be refined
    construct the next grid  $G_{k+1}$  only with elements with depth  $\leq t$ 
     $k += 1$ 
  until no new grid points with depth  $t$  are created
end for

```

result represents the physics correctly, but also all intermediate steps. As initial guesses for the velocity field \mathbf{u}^0 and p^0 on a refined grid structure G_{k+1} , we utilize the interpolated values from the results corresponding to the grid G_k . In the computation of the numerical results, we need about 5 refinement steps with fixed depth t until no new grid points are created.

4. Three-dimensional Lid-driven Cavity

This section provides numerical results for a flow driven by only one single (lid) plate. We present the underlying adaptive grids and discuss the computed flow patterns.

The two-dimensional lid-driven cavity has especially received considerable attention in the literature because of the complex flow characteristics exhibited in a relatively simple geometry. Therefore, it was, and still is, a popular example for testing and comparing numerical methods. This problem has been studied numerically using various techniques, including finite-difference, see e.g. [3, 13, 7, 6, 14], multi-grid, see e.g. [20, 1], spectral, see e.g. [16, 17], finite element, see e.g. [12] and integral equation methods, see e.g. [10, 8]. For the Stokes flow, analytical solutions based on eigenfunction expansions have been derived in [9, 18, 22]. An experimental apparatus and data are presented in [13]. The lid-driven cavity problem has also been of great interest as a test problem for evaluating numerical procedures for solving the Navier-Stokes equations.

In comparison with the two-dimensional case, there is only few literature for the three-dimensional lid-driven cavity, see e.g. [11, 23]. For a detailed discussion of similar three-dimensional problems (a cylindrical container and a disk-driven problem) see [19, 4]. The three-dimensional lid-driven cavity is in particular interesting, because the planar motion of the plate induces flow motion in the third dimension.

The flow geometry and the moving plate of the three-dimensional lid-driven cavity problem are displayed in Fig. 6. Analogical to the

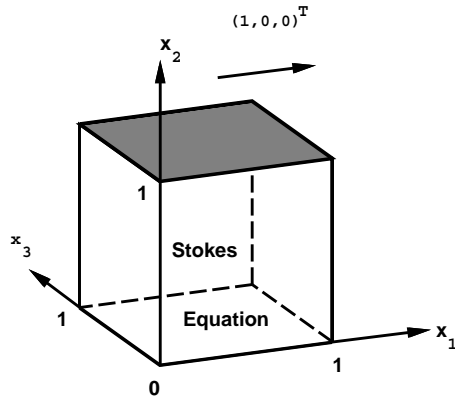


Fig. 6. The three-dimensional lid-driven cavity: geometry and moving plate in the lid plane $x_2 = 1$ in positive x_1 direction.

two-dimensional case, the flow is driven by the uniform translation in positive x_1 direction of a plate located in the lid plane $x_2 = 1$

$$(14) \quad \begin{aligned} \mathbf{u} &= (1, 0, 0)^T \text{ for } x_2 = 1 \text{ and} \\ \mathbf{u} &= \mathbf{0} \quad \text{for } x_1 = 0, x_1 = 1, x_2 = 0, x_3 = 0, \text{ or } x_3 = 1. \end{aligned}$$

Unfortunately, in this article, we can only give a short discussion of the results. We start with the underlying adaptive grid used in the computation. Fig. 7 shows a three-dimensional visualization of

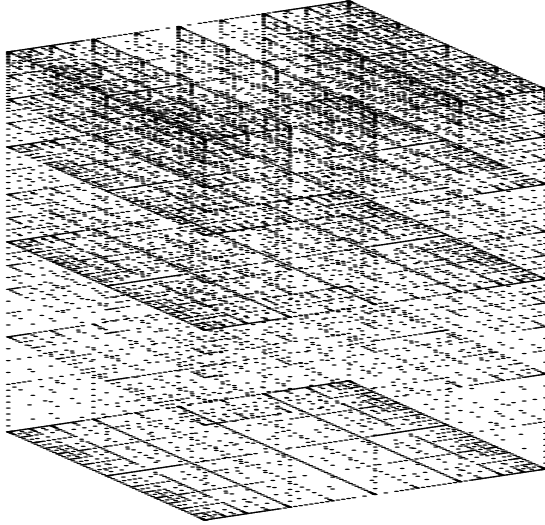


Fig. 7. The three-dimensional lid-driven cavity: adaptive grid (14 147 grid points). The lid plate is moving from left to right. (The coordinates are given in Fig. 6.)

an adaptive grid with 14 147 grid points. Fig. 8 shows four typical grids in the $x_1 - x_2$ -planes ($x_3 = 0, 8/64, 20/64$, and $31/64$). Due to the hierarchical approach, the number of grid points in the different planes is of different order of magnitude: 1361, 561, 223, and 30. We notice that there is a concentration of grid points next to the moving lid, especially along the two lines defined by $x_1 = 0, x_2 = 1$ and $x_1 = 1, x_2 = 1$. This is due to the singularity in the velocity boundary conditions (14). The qualitatively different resolution of

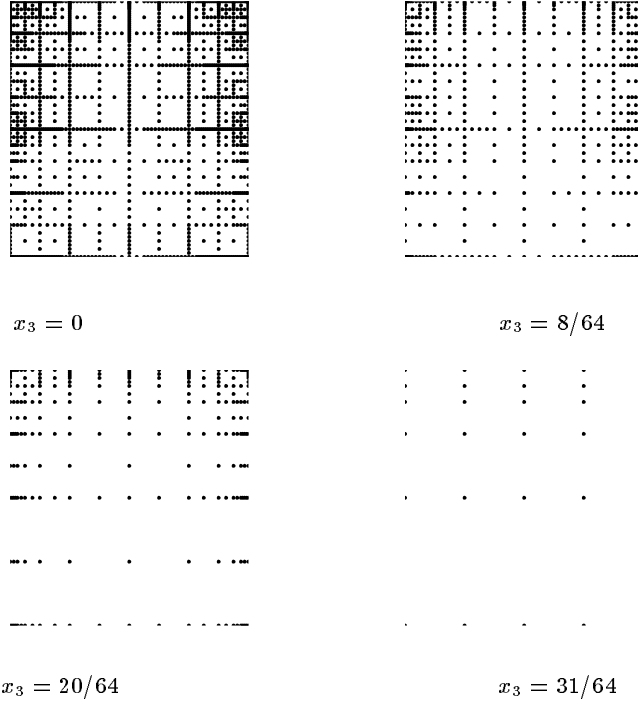


Fig. 8. The three-dimensional lid-driven cavity: grids in the $x_1 - x_2$ -planes with $x_3 = \text{const.}$ for $x_3 = 0, 8/64, 20/64, 31/64$ (1361, 561, 223, and 30 grid points). The lid is situated at the top and driven from left to right.

these line singularities is an important advantage of the hierarchical approach.

In order to get an idea of the three-dimensional flow, we display the velocity fields for the planes $x_i = \text{const}$ with $i = 1, 2, 3$. Note that the vectors in different plots are comparable, because they are not normalized.

First, we look at the velocity fields in the $x_1 - x_2$ -planes. Because the flow is symmetric about the plane $x_3 = 32/64$, we only show $x_1 - x_2$ -planes with $0 \leq x_3 \leq 1/2$. Fig. 9 provides the velocity fields for the $x_1 - x_2$ -planes with $x_3 = 2/64, 4/64, 8/64, 16/64$, and $32/64$. Next to the symmetry plane $x_3 = 32/64$, the flow pattern is similar to the two-dimensional case. The flow patterns are weakened by the resistance of the side plate, as one would expect. The deviation from the two-dimensional case is greatest near the side plate ($x_3 = 0$). In other word, the location of the primary vortex center and the norm of the velocity vectors depend on the variable x_3 .

Due to the more or less distinct primary vortex, the global flow structure is divided into a flow downstream area (half cube $x_1 > 1/2$) and a flow upstream area (half cube $x_1 < 1/2$). In the symmetry plane $x_1 = 1/2$, we expect no flow movement. This behaviour is exactly reflected in the plots of the velocity fields in the $x_2 - x_3$ -planes with $x_1 = 1/64, 16/64, 32/64, 48/64$, and $63/64$, see Fig. 10. Again, we observe the influence of the two non-moving plates in the planes $x_1 = 0$ and $x_1 = 1$: the strength of the flow is weakened towards the front and the back of the flow geometry.

From the discussion of the $x_1 - x_2$ - and the $x_2 - x_3$ -planes, we can imagine the flow as a (primary) rolling pin made of gum and fixed at the ends. This is also supported by the plots of the $x_1 - x_3$ -planes velocity fields, see Fig. 11. It is clear that next to the lid plate in the plane $x_2 = 1$, the flow is almost uniform in the positive x_1 direction, e.g. see the $x_1 - x_3$ -plane with $x_2 = 63/64$. In the $x_1 - x_3$ -plane with $x_2 = 48/64$, we can see that the vectors of the velocity field diverges from the symmetry axis $x_3 = 32/64$ next to the plate $x_1 = 1$. Whereas the vectors of the velocity field next to the plate $x_1 = 0$ converges into the parallel flow pattern. The recirculating flow at the bottom of the cube is displayed in the $x_1 - x_3$ -planes with $x_2 = 32/64$ and $1/64$. Still, we have convergence to the symmetry axis next to the plate $x_1 = 0$ and divergence next to the plate $x_1 = 1$. Again, the bottom plate $x_2 = 0$ weakens the strength of the flow. Next to both plates, the lid and the bottom plate, the vectors of the velocity field are almost parallel. Only in the region $x_2 \approx 43/64$, the nature of the flow differs qualitatively.

Actually, this is the region, where the main stream turns the direction from positive to negative x_1 -direction. It is very interesting that in between these parallel flow regions, two little vortices symmetric to the $x_3 = 1/2$ axis develop, see the $x_1 - x_3$ -plane $x_2 = 43/64$. A real three dimensional phenomenon! And, hereby, we want to close the discussion of the three-dimensional lid-driven cavity.

5. Concluding Remarks

In this paper, we have developed a solution method for the Stokes equations in the formulation of the primitive variables. Because, we use a pressure correction scheme, we end up with Algorithm 1 “Successive Poisson Equation”. We discretize these Poisson equations with the tools of the adaptive hierarchical finite element method, presented in [15]. In order to satisfy the divergence equation, we use the hierarchical surplus of the weak divergence (13) as adaptation criterion.

For the solution of the arising systems of linear equations, we apply the multigrid solver, see also [15]. To ensure that not only the final, but also all intermediate steps of the adaptation process, give the physics correctly, we perform Algorithm 2 “Adaptive Stokes”. Here, we fix the depth t for the refinement steps, until no new grid points are created. Afterwards, we increase the allowed maximum depth t by 1.

The discussion of the numerical results shows that the primary flow structures for the different examples are given correctly, even for coarse discretizations. All results are quite satisfying and very encouraging.

In the opinion of the authors, there is a huge potential in the method of adaptive hierarchical tensor product finite elements. However, there are, at least, three main subjects of future work. First, we have to speed up the outer iteration, because then we can use much finer discretizations. This is necessary for the accuracy of the solutions. Second, we have to implement different adaptation criteria, in order to resolve more details of the flow patterns, e.g. the counterrotating secondary eddies. In the context of adaptation, it might also be of interest to refine the velocity components and the pressure separately, leading to different grid structures. Finally, we must design a robust Navier-Stokes solver. In a first attempt, we calculated solutions of the two-dimensional driven cavity with Reynolds number $Re = 30$.

References

1. C.-H. Bruneau and C. Jouron (1990): An efficient scheme for solving steady incompressible Navier-Stokes equations, *J. Comput. Phys.*, **89**, 389–413.
2. H.-J. Bungartz (1998): Finite elements of higher order on sparse grids, *Habilitationsschrift*, Institut für Informatik, TU München.
3. O. R. Burggraf (1993): Analytical and numerical studies of the structure of steady separated flows, *J. Fluid Mech.*, **24**, 113–151.
4. T. P. Chiang, W. H. Sheu, and S. F. Tsai (1999): Disk-driven vortical flow structure in a cubical container, *Computers and Fluids*, **28**, 41–61.
5. G. Faber (1909): Über stetige Funktionen, *Mathematische Annalen*, **66**, 81–94.
6. M. M. Gupta (1991): High accuracy solutions of the Navier-Stokes equations, *J. Fluid Mech.*, **93**, 343–359.
7. M. M. Gupta and R. P. Manohar (1979): Boundary approximations and accuracy in viscous flow computations, *J. Comput. Phys.*, **31**, 265–288.
8. E. B. Hansen and M. A. Kelmanson (1992): Integral equation analysis of the driven cavity boundary singularity, *Appl. Math. Lett.*, **5**, 15–19.
9. D. D. Joseph and L. Sturges (1978): The convergence of biorthogonal series for biharmonic series for biharmonic and Stokes flow edge problems: Part II, *Siam J. Appl. Math.*, **34**, 7–26.

10. M. A. Kelmanson (1983): Modified integral equation solution of viscous flows near sharp corners, *Computers and Fluids*, **11**, 307–324.
11. H. C. Ku, R. S. Hirsh, and T. D. Taylor (1987): A pseudospectral method for solution of the three-dimensional incompressible Navier-Stokes equations, *Journal of Computational Physics*, **70**, 439–462.
12. J. T. Oden and L. Demkowicz (1991): h - p adaptive finite element methods in computational fluid dynamics, *Computer Meth. in Appl. Mech. and Eng.*, **89**, 11–40.
13. F. Pan and A. Acrivos (1967): Steady flows in rectangular cavities, *J. Fluid Mech.*, **28**, 643–655.
14. T. Schiekofer (1998): Die Methode der finiten Differenzen auf dünnen Gittern zur adaptiven Multilevel-Lösung partieller Differentialgleichungen, Dissertation, Mathematisch-Naturwissenschaftliche Fakultät, Rheinische Friedrich-Wilhelms-Universität Bonn.
15. S.-A. H. Schneider (2000): Adaptive solution of elliptic partial differential equations by hierarchical tensor product finite elements, Dissertation, Institut für Informatik, TU München.
16. W. W. Schultz, N. Y. Lee, and J. P. Boyd (1989): Chebyshev pseudospectral method of viscous flows with corner singularities. *J. Sci. Comput.*, **4**, 1–24.
17. M. R. Schumack, W. W. Schultz, and J. P. Boyd (1991): Spectral method solution of the Stokes equations on nonstaggered grids. *J. Comput. Phys.*, **94**, 30–58.
18. P. N. Shankar (1993): The eddy structure in Stokes flow in a cavity, *J. Fluid Mech.*, **250**, 371–383.
19. P. N. Shankar (1997): Three-dimensional eddy structure in a cylindrical container, *J. Fluid Mech.*, **342**, 97–118.
20. W. Shyy and C.-S. Sun (1993): Development of a pressure correction/staggered-grid based multigrid solver for incompressible recirculating flows, *Computers and Fluids*, **22**, 51–76.
21. K. Simony (1990): *Kulturgeschichte der Physik*. Akadémiai Kiadó, Budapest.
22. T. Stöerckuhl, C. Zenger, and S. Zimmer (1992): An asymptotic solution for the singularity at the angular point of the lid driven cavity, Report TUM-19235, Institut für Informatik, TU München.
23. C. M. Teixeira (1997): Digital physics simulation of the lid-driven cavity flow, *Inter. J. of Modern Physics C*, **8**.
24. H. Yserentant (1986): On the multi-level splitting of finite element spaces, *Numer. Math.*, **49**, 379–412.
25. C. Zenger (1991): Sparse Grids, in: *Parallel Algorithms for Partial Differential Equations* (W. Hackbusch, ed.), volume **31** of NNFM, Vieweg, Braunschweig/Wiesbaden.

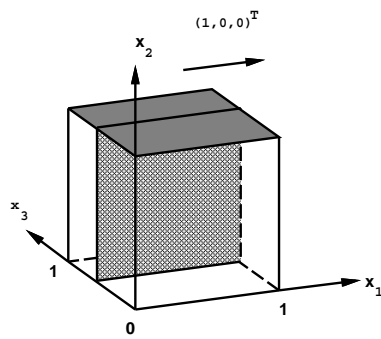
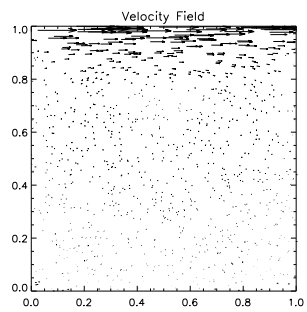
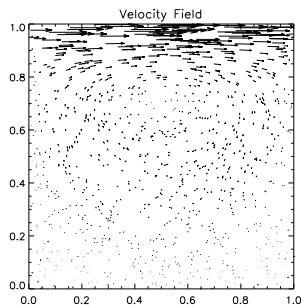
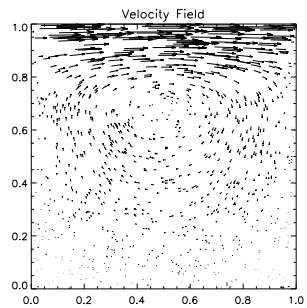
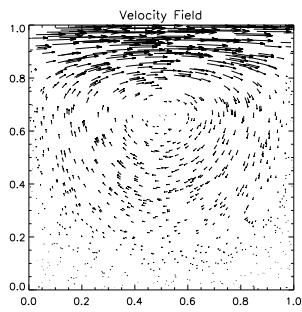
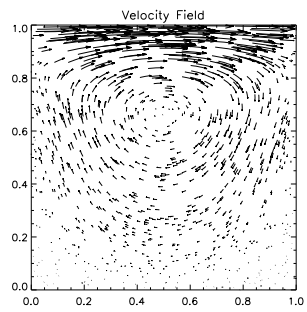
 $x_1 - x_2$ -plane-indicator $x_3 = 2/64$  $x_3 = 4/64$  $x_3 = 8/64$  $x_3 = 16/64$  $x_3 = 32/64$

Fig. 9. The three-dimensional lid-driven cavity: the plane-indicator (above left) shows the orientation of the $x_1 - x_2$ -planes with $x_3 = 2/64, 4/64, 8/64, 16/64$, and $32/64$.

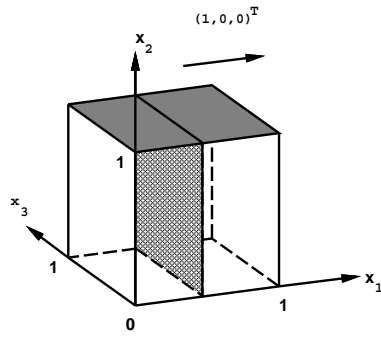
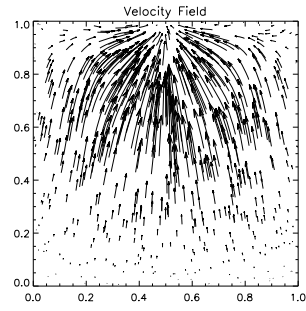
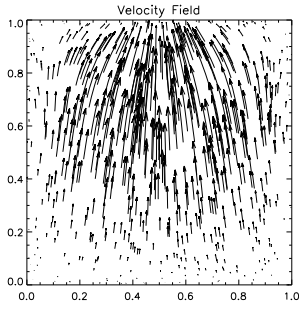
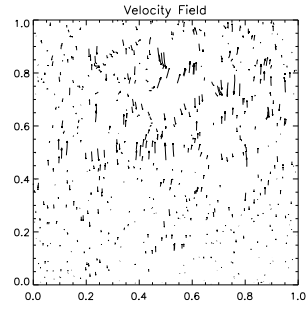
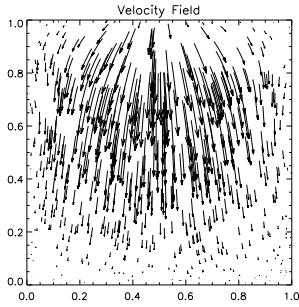
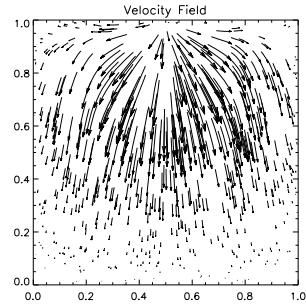
 $x_2 - x_3$ -plane-indicator $x_1 = 1/64$  $x_1 = 16/64$  $x_1 = 32/64$  $x_1 = 48/64$  $x_1 = 63/64$

Fig. 10. The three-dimensional lid-driven cavity: the plane-indicator (above left) shows the orientation of the $x_2 - x_3$ -planes with $x_1 = 1/64, 16/64, 32/64, 48/64$, and $63/64$.

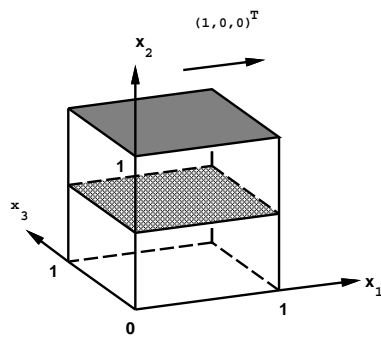
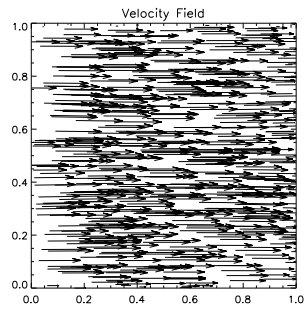
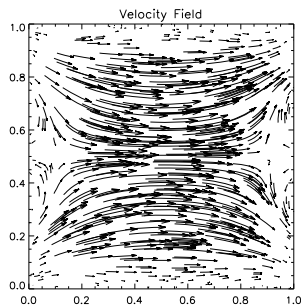
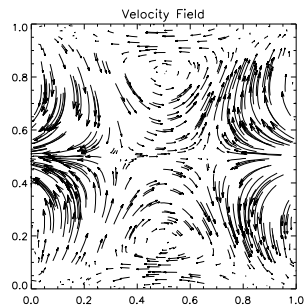
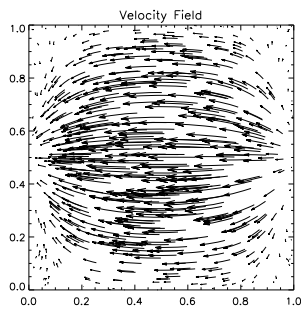
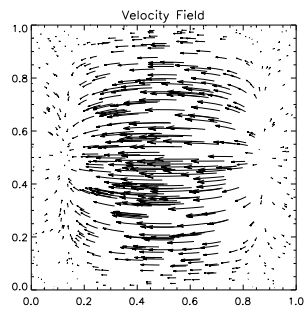
 $x_1 - x_3$ -plane-indicator $x_2 = 63/64$  $x_2 = 48/64$  $x_2 = 43/64$  $x_2 = 32/64$  $x_2 = 1/64$

Fig. 11. The three-dimensional lid-driven cavity: the plane-indicator (above left) shows the orientation of the $x_1 - x_3$ -planes with $x_2 = 63/64, 48/64, 43/64, 32/64$, and $1/64$.